Ceramics International 51 (2025) 53354–53368

Contents lists available at ScienceDirect

Ceramics International

journal homepage: www.elsevier.com/locate/ceramint

Structural, optical, and dielectric studies on transition metals doping (Cu, Ni) in $MgFe_2O_4$ ferrites

Siwar Dhahri [a,b], Aref Omri [a], Mohamed Houcine Dhaou [c], Essebti Dhahri [d], Manuel P.F. Graça [e], Anna B. Brito [f], Rui Fausto [f,g], João Pina [f], Benilde F.O. Costa [b,*]

[a] Laboratory of Advanced Multifunctional Materials and Technological Applications, Faculty of Science and Technology of Sidi Bouzid, Campus Agricultural City, Sidi Bouzid, 9100, University of Kairouan, Tunisia
[b] University of Coimbra, CFisUC, Physics Department, Rua Larga, 3004-516, Coimbra, Portugal
[c] Department of Physics, College of Science, Qassim University, Saudi Arabia
[d] Laboratory of Applied Physics, Faculty of Sciences, University of Sfax, P.O. Box 1171, 3000, Sfax, Tunisia
[e] I3N and Physics Department, University of Aveiro, 3810-193, Aveiro, Portugal
[f] University of Coimbra, CQC-IMS, Chemistry Department, 3004-535, Coimbra, Portugal
[g] Spectroscopy@IKU, Faculty of Sciences and Letters, Department of Physics, Istanbul Kultur University, Ataköy Campus, Bakırköy, 34156, Istanbul, Türkiye

ARTICLE INFO

Handling editor: Dr P. Vincenzini

Keywords:
Spinels
Sol-gel synthesis
Optical bandgap
Urbach energy
CBH model
Energy storage
Dielectric constant

ABSTRACT

Spinel ferrites are increasingly researched for their tunable optical and electrical properties, with applications in electronic devices and microwave absorption. This study investigates $Mg_{0.5}Cu_{0.3}Ni_{0.2}Fe_2O_4$ synthesized via sol-gel auto-combustion, yielding a single-phase cubic spinel structure (Fd-3m) with crystallite sizes of ~1.1 μm. XRD and Raman spectroscopy confirmed the phase purity and identified five active modes (A_1g, Eg, $3T_2g$). Optical analysis revealed a direct bandgap (Eg = 2.335 eV), low Urbach energy (Eu = 0.2386 eV), and strong UV–Vis absorption, indicating high crystallinity and suitability for optoelectronics. Electrical measurements demonstrated semiconducting behavior with an activation energy (Ea) of 0.34 eV, governed by the Correlated Barrier Hopping (CBH) model. Dielectric studies showed high permittivity ($\varepsilon' > 10^3$ at low frequencies) and significantly reduced loss (tan $\delta < 0.1$ at 10^6 Hz), confirming efficacy in high-frequency energy transmission/storage. The synergistic Cu/Ni doping enables tailored structural, optical, and dielectric properties, positioning this material as a promising candidate for high-frequency electronics, energy storage systems, and solar cells.

1. Introduction

Electrical and dielectric materials are attracting growing interest owing to their multifunctional properties and broad range of technological uses. Among these materials, spinel ferrites stand out for their unique combination of advantageous characteristics, including high dielectric permittivity, low electrical conductivity, excellent thermal and chemical stability, and strong adsorption ability [1,2]. These properties place them at the forefront of research for deployment in electronic devices, sensors, high-frequency capacitors, and electrical insulation materials [3].

The optical and electrical properties of spinel ferrites are intimately associated with their crystalline structure, usually denoted by the general formula MFe_2O_4, where M stands for a transition metal cation. The arrangement of M and Fe ions within the crystal lattice can result in either cubic or tetragonal symmetry, which directly influences their dielectric behavior. The specific identity of the M-site cation significantly affects critical features such as electrical conductivity, dielectric constant, and dielectric loss, ultimately determining the material's application performance like low-loss electronic components, electromagnetic wave absorbers, and functional coatings [4].

Thanks to their distinct electrical, optical, and chemical properties, spinel ferrites are increasingly being explored for advanced applications such as capacitive sensors, dielectric filters, electrical insulators, and optical devices [3,5,6]. Their chemical stability and compatibility with emerging technologies further position them as promising materials for next-generation electronics and optoelectronics. Additional applications span across spintronic devices, magnetic storage systems, transformer cores, nanophotocatalysis, ferrofluids, and biomedical technologies like targeted drug delivery and magnetic hyperthermia [7–9].

* Corresponding author.
E-mail address: benilde@uc.pt (B.F.O. Costa).

https://doi.org/10.1016/j.ceramint.2025.09.084
Received 27 June 2025; Received in revised form 15 August 2025; Accepted 4 September 2025
Available online 5 September 2025

Various synthesis techniques, including the sol-gel method [10], hydrothermal synthesis, and co-precipitation, enable accurate control of the chemical composition, size, and morphology of spinel ferrites. The sol-gel method is distinguished for its simplicity, low cost, and capacity to yield homogeneous materials with optimized properties for electronic and optoelectronic uses. This widely adopted technique allows for uniform particle distribution, reduced processing temperatures and annealing times, and fine control over the material's final characteristics, thereby facilitating significant advances in spinel ferrite research [11,12].

Several recent studies on Ni doped- Mg and Ni-Cu co-doped ferrites are found in literature [13–18]. Structural, dielectric, electrical and magnetic properties were the aim of those studies.

In this context, the present work contributes to the ongoing research on doped ferrites by focusing on the $Mg_{0.5}Cu_{0.3}Ni_{0.2}Fe_2O_4$ system, a member of the MFe_2O_4 spinel family. The simultaneous substitution of Cu and Ni cations offers synergistic effects that modulate the structural and dielectric properties of the material. While Cu^{2+} tends to introduce local lattice distortions due to its electronic configuration and larger ionic radius, Ni^{2+} enhances structural stability and may improve magnetic behavior. This dual doping strategy enables precise tuning of cation distribution between tetrahedral and octahedral sites, which in turn affects interfacial polarization, electrical conductivity, and dielectric response. As such, this study not only explores a novel material composition but also provides insights relevant to the design of ferrites with tailored functionalities for sensors, energy storage, and optoelectronic devices.

The structural characteristics of $Mg_{0.5}Cu_{0.3}Ni_{0.2}Fe_2O_4$, particularly crystallite size and phase distribution, are essential for determining its optical and dielectric performance. The analysis of the crystalline structure using X-ray diffraction (XRD) provides information on the material's quality, while scanning electron microscopy (SEM) and UV–Vis spectroscopy offer detailed insights into its morphology and optical properties, such as absorption in the UV–visible range. These properties are particularly important for applications in optoelectronic devices and optical sensors [13,14]. Simultaneously, the material's dielectric behavior – namely dielectric constant, dielectric loss, and frequency dependence - plays a key role in its potential use in energy storage systems and high-frequency electronics.

In conclusion, the synthesis of $Mg_{0.5}Cu_{0.3}Ni_{0.2}Fe_2O_4$ spinel ferrite via the sol-gel technique and an investigation of its structural, optical, and dielectric characteristics provide crucial insights for its integration into advanced applications in electronics and optoelectronics. This study aims to elucidate the relationship between synthesis parameters and material functionality, ultimately guiding its use in cutting-edge technological innovations.

2. Experimental

2.1. Synthesis procedure

$Mg_{0.5}Cu_{0.3}Ni_{0.2}Fe_2O_4$ ferrites were synthesized via sol-gel auto-combustion to produce pure, high-density powders with uniform grain sizes. High-purity precursors—$Mg(NO_3)_2{\cdot}6H_2O$ (1.76 g), $Cu(NO_3)_2{\cdot}3H_2O$ (0.99 g), $Ni(NO_3)_2{\cdot}6H_2O$ (0.80 g), and $Fe(NO_3)_3{\cdot}9H_2O$ (11.08 g), were dissolved in 100 mL deionized water and stirred at 90 °C until homogeneous. Citric acid ($C_6H_8O_7{\cdot}H_2O$, M = 210.139 g/mol) was added as a chelating agent at a 1:1 M ratio with total metal ions (Mg^{2+} + Cu^{2+} + Ni^{2+} + Fe^{3+}). The solution was stirred at 80 °C for 1 h, and the pH was adjusted to 7.0 using ammonia solution (NH_4OH) to optimize metal complexation.

Ethylene glycol ($C_2H_6O_2$, M = 62.08 g/mol, 11.238 mL) was then incorporated as a fuel at a 2:1 M ratio relative to citric acid to promote auto-combustion. The mixture was heated to 250 °C in a ventilated furnace, triggering self-sustaining combustion that produced a brown-colored foam. The foam was crushed into a fine powder (<50 μm particle size) using an agate mortar.

The powder underwent successive calcination at 600 °C and 800 °C for 12 h each, with intermediate grinding to eliminate organic residues. Finally, the powder was pressed into cylindrical pellets (8 mm diameter; 1–2 mm thickness) under 5-ton pressure and sintered at 1000 °C for 24 h in air to achieve densification.

2.2. Experimental characterization techniques

Structural characterization was conducted using powder X-ray diffraction (XRD) with a BRUKER D8 diffractometer equipped with a CuKα radiation source (λ = 1.5406 Å) in Bragg-Brentano geometry (θ -2θ). The scans covered an angular range from 20° to 100° with a step size of 0.02° and an acquisition time of 1 s per step. The obtained X-ray diffraction data were subsequently analysed using Rietveld refinement with the FULPROF program [15].

Powder morphology and elemental composition were characterized using scanning electron microscopy (SEM) together with energy-dispersive X-ray spectroscopy (EDS), employing a TESCAN VEGA3 SGH microscope.

Vibrational properties of the powders were examined using a Raman spectrometer (Horiba LabRam HR Evolution) using a Synapse CCD detector, a BXFM open-space confocal microscope, and a 600 g/mm grating, utilizing an excitation of 532 nm.

The solid-state absorption spectra of the powders were obtained by collecting the diffuse reflectance using a Shimadzu UV-2600i spectrophotometer with an ISR-2600Plus integrating sphere (220–1400 nm range). Background correction was done using $BaSO_4$ as reference prior to the determination of the spectra of the samples. Conversion to absorption was performed assuming the Kubelka-Munk function, F(R) [16]. Photoluminescence spectra of the powder were collected in front-face using a Horiba-Jobin-Yvon Fluorolog 3.2.2 spectrometer.

Thermal analysis was conducted, from 30 °C to 500 °C, using Differential Scanning Calorimetry (DSC) with a PerkinElmer STA6000, operating at a rate of 10 °C/min under nitrogen atmosphere. This system measures both the sample and the reference simultaneously, which offers a distinct advantage.

The electrical and dielectric properties of $Mg_{0.5}Cu_{0.3}Ni_{0.2}Fe_2O_4$ $_4$ were studied using impedance spectroscopy with an *Agilent* 4294A analyzer. Capacitance, conductance, and impedance studies were performed under vacuum and without light exposure, using silver disks in a planar capacitor configuration. The study was conducted over a frequency range from 40 to 10^6 Hz and a temperature range between 250 and 350 K.

3. Results and discussions

3.1. Structural studies

The XRD diffractogram of the $Mg_{0.5}Cu_{0.3}Ni_{0.2}Fe_2O_4$ sample is presented in Fig. 1, along with the refinement of crystal structure using the Rietveld method. The peak shapes in the diffraction pattern were modelled using a pseudo-Voigt function [17]. The refinement process was iterated until a goodness of fit close to 1 was achieved, confirming the reliability of the refinement model. In Fig. 1 the indexation of the diffraction peaks is also shown to the characteristic reflections of the cubic spinel structure (ICDD 88–0671) in line with the *Fd-3m* space group. Additionally, the XRD data reveals a homogeneous crystallization of the sample, showing a single phase with no other secondary phases. Table 1 summarizes the structural parameters, such as unit cell dimensions, atomic positions, and site occupancies, derived from the XRD data.

In this analysis, it is crucial to consider the distribution of cations between the tetrahedral (A) and the octahedral [B] sites of the $Mg_{0.5}Cu_{0.3}Ni_{0.2}Fe_2O_4$ sample. We have considered that Mg^{2+}, Cu^{2+}, and Ni^{2+} ions predominantly occupy octahedral [B] sites, whereas Fe^{3+} ions

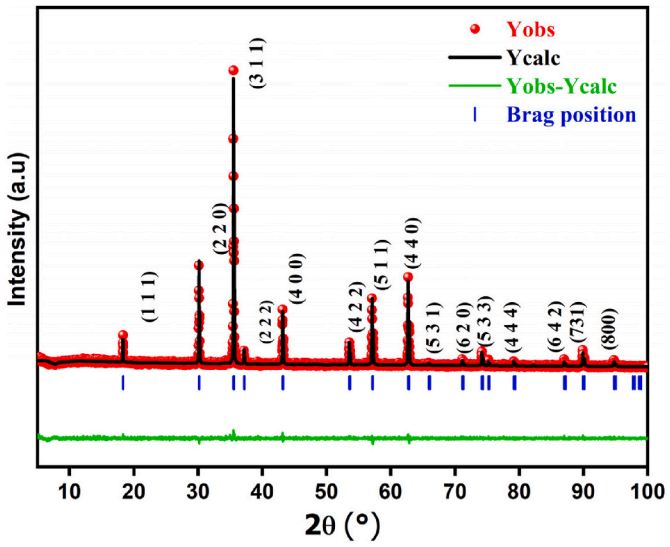

Fig. 1. The refined XRD pattern of $Mg_{0.5}Cu_{0.3}Ni_{0.2}Fe_2O_4$ sample, with Miller indexes of the spinel cubic structure.

Table 1
Results of the Rietveld refinement.

Space Group	Fd3-m		
Lattice Parameters	***a* (Å)**		8.37468
	***V* (Å^3)**		587.360
Atoms	Fe	**Wyckoff Positions**	8a
		Atomic x = y = z	1/8
		Occupancy Factors	1
		B_{iso} (Å^2)	1.968
	Mg/Cu/Ni/Fe	**Wyckoff Positions**	16d
		Atomic x = y = z	1/2
		Occupancy Factors	0.5/0.3/0.2/1
	O	**Wyckoff Positions**	32e
		Atomic x = y = z	0.25797
		Occupancy Factors	4
Structural Parameters	R_A (Å)		1.92
	R_B (Å)		6.86
	θ_A (°)		24.23°
	θ_B (°)		151.50°
Agreement Factors	R_p (%)		17
	R_{wp} (%)		17.7
	R_F(%)		5.60
	χ^2 (%)		0.8

are dispersed across both A and B sites. Thus, the cation distribution for $Mg_{0.5}Cu_{0.3}Ni_{0.2}Fe_2O_4$ can be described as $(Fe_1^{3+})A[Mg_0^{2+}.{}_5Cu_0^{2+}.{}_3Ni_0^{2+}.{}_2Fe_1^{3+}]B\ O_4^{2-}$. Structural refinement was performed with FullProf software, based on this formula. The [B] cations, [A] cations, and oxygen atoms were assigned to the 16d (1/2, 1/2, 1/2), 8a (1/8, 1/8, 1/8), and 32e (x, y, z) Wyckoff positions, respectively. This arrangement showcases the tetrahedral and octahedral coordination with oxygen, leading to the formation of the inverse spinel structure.

Regarding the effect of Cu^{2+} and Ni^{2+} substitution on the lattice, these cations partially replace Mg^{2+} and Fe^{3+} ions in the spinel framework. Given their ionic radii—Cu^{2+} (0.73 Å) and Ni^{2+} (0.69 Å) compared to Mg^{2+} (0.72 Å) and Fe^{3+} (0.645 Å) for octahedral coordination—the substitution induces subtle lattice distortions reflected by slight shifts in the diffraction peak positions. Particularly, Cu^{2+} ions, preferring octahedral sites, can generate local distortions through Jahn-Teller effects, causing elongation or compression of octahedral bond lengths. Ni^{2+} ions, due to their relatively smaller size, tend to contract the lattice parameter and introduce strain within the crystal lattice.

Fig. 2, generated using the VESTA software [18] based on the Rietveld-refined output of $Mg_{0.5}Cu_{0.3}Ni_{0.2}Fe_2O_4$, provides a detailed

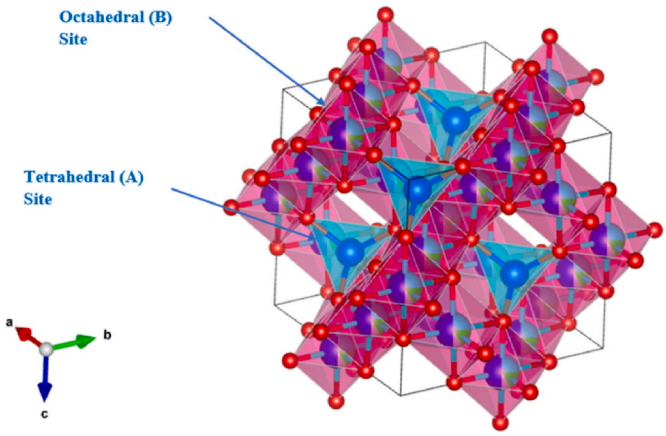

Fig. 2. Unit cell representation with tetrahedral and octahedral sites of $Mg_{0.5}Cu_{0.3}Ni_{0.2}Fe_2O_4$.

visualization of this structural configuration.

Table 2 presents the structural variables obtained at room temperature for the compound studied. For the determination of the crystallite size (D) two methods were used: Debye-Scherrer and the modified Debye-Scherrer plot, as illustrated in Fig. 3. The equations used are $D = \frac{0.9\,\lambda}{\beta\cos\theta}$ and $ln\,\beta = ln\left(\frac{0.9\lambda}{D}\right) + ln\left(\frac{1}{\cos\theta}\right)$, respectively, where λ represents the wavelength of incident beam, θ is the Bragg angle and β is the full width at half maximum (FWHM) of the diffraction peak. For the first method, the FWHM of the most intense diffraction peak (311), determined using a Gaussian function, was used, while the straight-line fit of Fig. 2 gives the crystallite size in the second method [19]. This modification addresses one of the key limitations of the conventional Scherrer equation, which assumes cos(θ) constant across different diffraction angles, potentially leading to errors at higher 2θ values.

The X-ray density (ρ_x) was calculated, assuming that a cubic spinel structure contains eight molecules per unit cell, using the formula:

$$\rho_X = \frac{8M}{Na^3} \tag{1}$$

in this equation, N is Avogadro's number, M the molecular weight of the ferrite, and a the lattice constant obtained from XRD measurements.

The apparent density of $Mg_{0.5}Cu_{0.3}Ni_{0.2}Fe_2O_4$ was calculated using the standard relation

$$\rho_b = \frac{m}{h\pi r^2} \tag{2}$$

where m is the mass, r the radius, and h the thickness, of the sintered pellet.

The porosity percentage was determined from the experimental density and the X-ray density, by the formula:

$$P = \left(1 - \frac{\rho_b}{\rho_X}\right) \times 100 \tag{3}$$

The specific surface area (S_a) can be determined using the following expression, where Ds_C is the crystallite size in nanometers, determined

Table 2
Structural parameters obtained at room temperature for the studied compound.

Crystallite size (Scherrer method) (nm)	Dsc	52.38
Crystallite size (Modified Scherrer method) (nm)	D	41.95
Density (g cm^3)	ρ_{XRAY}	4.94(3)
Bulk density (g cm^3)	ρ_{exp}	4.73(3)
Porosity (%)	P	4.28(3)
Specific surface area (m^2 g^{-1})	S_a	25.62 (3)

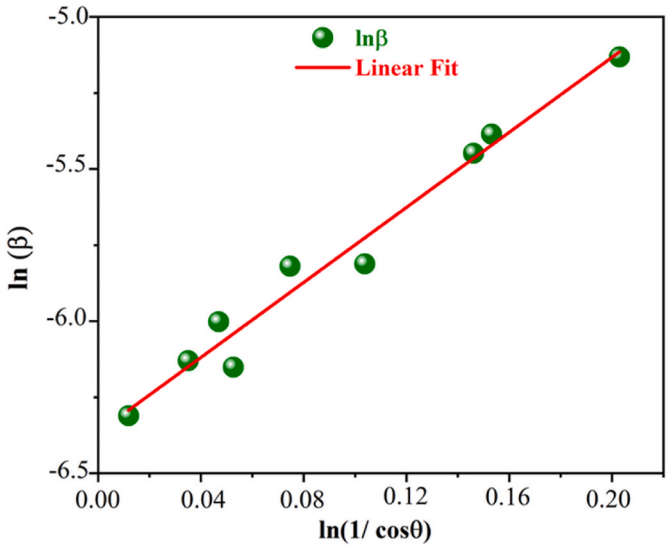

Fig. 3. Modified Debye-Scherrer plot.

from the classical Debye-Scherrer model, and ρ_x is the particle density in g/cm^3.

$$S_a = \frac{6000}{D_{sc}\rho_X} \quad (4)$$

All the parameters derived from these calculations are presented in Table 2. The specific surface area and porosity significantly influence the properties of polycrystalline spinel ferrites.

Fig. 4 presents the SEM image on the sample surface. In Fig. 4a, the Lorentzian fit applied to the histogram indicates a mean grain size of approximately 1.1 μm for the synthesized $Mg_{0.5}Cu_{0.3}Ni_{0.2}Fe_2O_4$ compound. The SEM micrograph shown in Fig. 4b reveals significant grain agglomeration, with large facets dominating the structure. Grain size analysis was conducted via ImageJ software based on several SEM images taken of the surface of the sample.

Energy Dispersive X-ray Spectroscopy (EDS) was performed to check on elemental analysis. Fig. 5 shows the EDS pattern and area mapping for the sample studied. The EDS spectrum reveals peaks corresponding to the elemental composition of the investigated sample, confirming the presence of all the starting elements used in the preparation of $Mg_{0.5}Cu_{0.3}Ni_{0.2}Fe_2O_4$ (Mg, Cu, Ni, Fe, and O) and also assuring the pretended composition. Moreover, the EDS area mapping shows that all elements are uniformly dispersed across the material. Table 3 shows the elementary composition for the compound

Raman spectroscopy is widely used as a powerful tool for a more in-depth analysis of structural properties. It is particularly effective in examining short-range cationic disorder due to its high sensitivity and excellent spatial resolution, which are essential for probing vibrational modes in spinel ferrites [20].

Fig. 6 displays the room-temperature Raman spectrum of $Mg_{0.5}Cu_{0.3}Ni_{0.2}Fe_2O_4$ within the 150–850 cm^{-1} frequency range, and using 520 nm laser. In the Fd-3m space group characteristic of spinel structures there are five Raman-active modes at ambient conditions: A1g + Eg + 3T2g. The notation is defined as: A (1D), E (2D), T (3D), with g indicating symmetry about the inversion centre [21]. In Fig. 6 the lines are Lorentzian fits of the spectrum, allowing the determination of the frequency of the five Raman active modes. The bands appear well-defined, reflecting the structural characteristics of the spinel lattice and confirming the spinel structure (Fd-3m space group) of the synthesized ferrite. The most intense Raman bands appear around 322 cm^{-1}, 472 cm^{-1}, and 698 cm^{-1}, corresponding to the Eg, T2g(2), and A1g modes, respectively. Additionally, minor bands are detected near 200 cm^{-1} and 550 cm^{-1}, assigned to the T2g(1) and T2g(3) modes, as illustrated in Table 4. These last vibrational modes arise from metal-oxygen bond stretching, with Eg and T2g modes are ascribable to asymmetric stretching vibrations within octahedral coordination, while the A1g mode corresponding to symmetric stretching in tetrahedral sites. In the spectrum of the studied material, a slight spectral shift is observed towards lower shift values, when it is compared with the spectrum of pure magnesium ferrite [21], due to influence of the distinct *radii* of the dopant metal atoms on both the bond lengths and strength of metal-oxygen bonds).

3.2. Thermal analysis

The thermal behavior of the $Mg_{0.5}Cu_{0.3}Ni_{0.2}Fe_2O_4$ ferrite sample was investigated by Differential Scanning Calorimetry (DSC) in the temperature range of 50 °C–500 °C, as shown in Fig. 7. Two prominent endothermic peaks are observed at approximately 450 K (177 °C) and 615 K (342 °C). Similar thermal features have been reported in substituted spinel ferrites, where cation distribution and chemical composition strongly influence magnetic and structural transitions [22].

The first peak near 450 K can be attributed to the ferrimagnetic-to-paramagnetic transition (Curie transition), which is known to occur around this temperature in certain substituted magnesium ferrites, such as $Mg(Fe_{0.8}Ga_{0.2})_2O_4$ [23]. This suggests that the combined Cu and Ni substitutions in our sample shift the Curie temperature downwards from that of pure $MgFe_2O_4$.

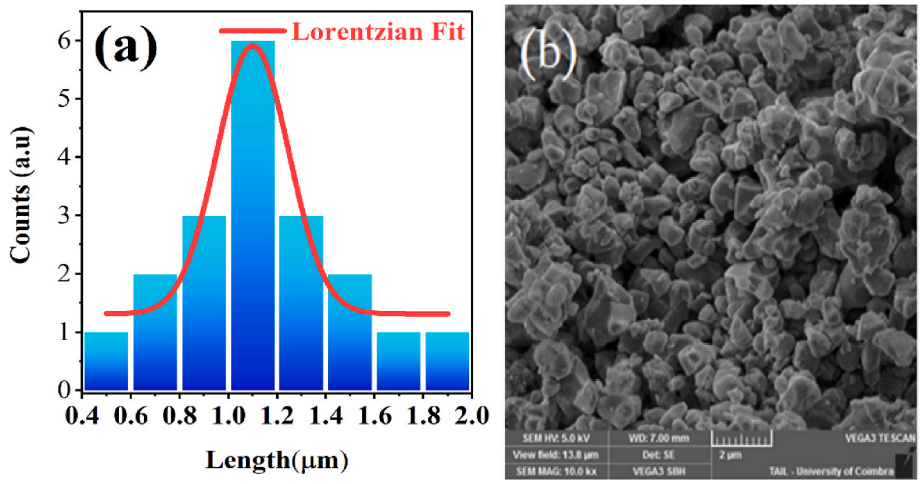

Fig. 4. (a) Grain size histogram of SEM particles, **(b)** SEM micrograph of Mg $_{0.5}Cu_{0.3}Ni_{0.2}Fe_2O_4$ surface.

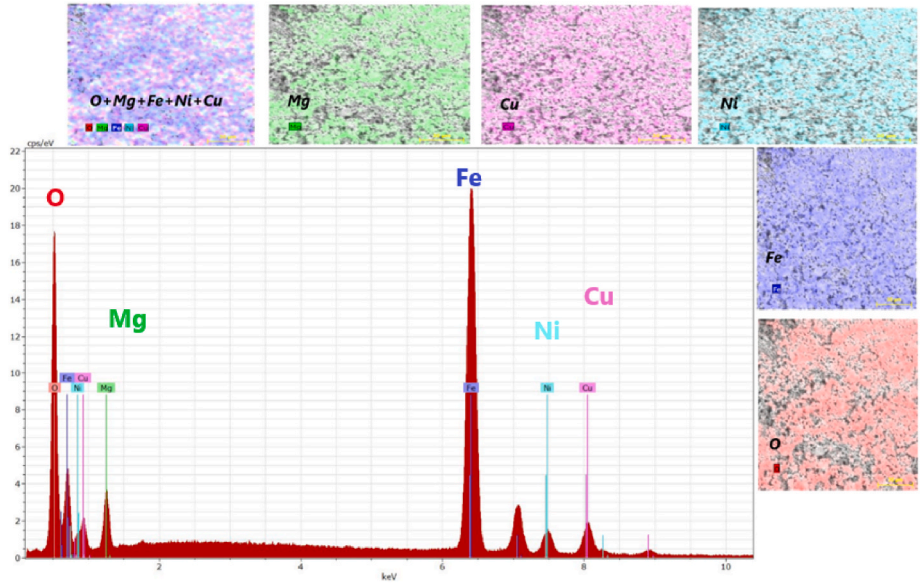

Fig. 5. EDS spectrum and elemental mapping of $Mg_{0.5}Cu_{0.3}Ni_{0.2}Fe_2O_4$.

Table 3
Composition (in atomic percentage) of compound.

Element	Experimental values %	Theoretical values %
Mg	6.84	7.4
Cu	4.38	4.28
Ni	2.82	2.85
Fe	32.72	28.57

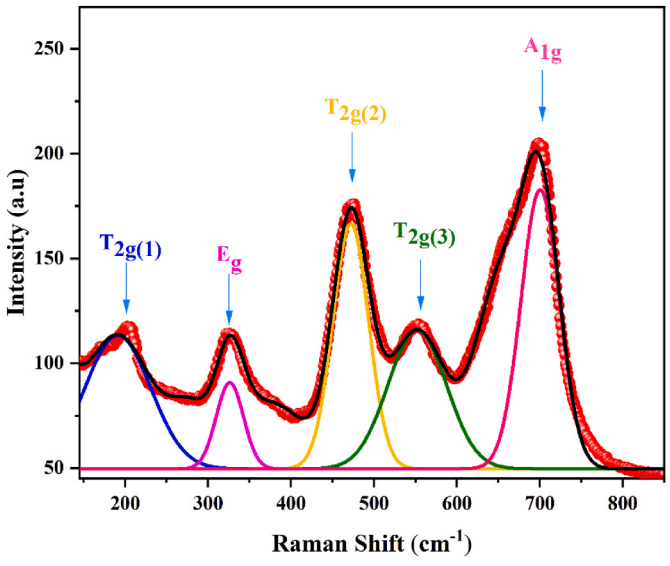

Fig. 6. Room-temperature Raman spectrum of $Mg_{0.5}Cu_{0.3}Ni_{0.2}Fe_2O_4$.

Table 4
Vibration modes and their Raman shifts.

Mode	Shift (cm^{-1})
T_{2g} (1)	200
E_g	322
T_{2g} (2)	472
T_{2g} (3)	550
A_{1g}	698

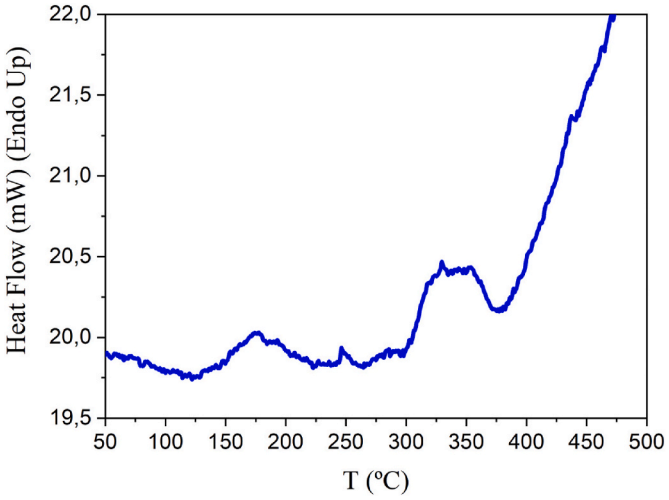

Fig. 7. Heat flow curve, as obtained from DSC measurements, in function of temperature.

The second endothermic peak at approximately 615 K may correspond to cation redistribution within the spinel lattice or subtle structural rearrangements, such as a tetragonal-to-cubic phase transition, which has been reported in related Cu-containing ferrites. Such transitions affect the lattice symmetry and can influence the material's magnetic and dielectric properties.

These findings demonstrate the important role of cation doping on the thermal stability and functional behavior of $Mg_{0.5}Cu_{0.3}Ni_{0.2}Fe_2O_4$ ferrites [23].

3.3. Optical studies

Fig. 8 (a) illustrates the absorbance *A* for the spinel ferrite $Mg_{0.5}Cu_{0.3}Ni_{0.2}Fe_2O_4$ across the UV (ultraviolet), VIS (visible), and NIR (near-infrared) regions, calculated from the diffuse reflectance of the sample using the Kubelka-Munk equation [16]. The spectrum shows strong absorption in the UV and VIS regions, which decreases sharply beyond 800 nm, showing minimal absorption in the infrared range. This behavior can be ascribed to electronic excitations between O^{2-} (2p)

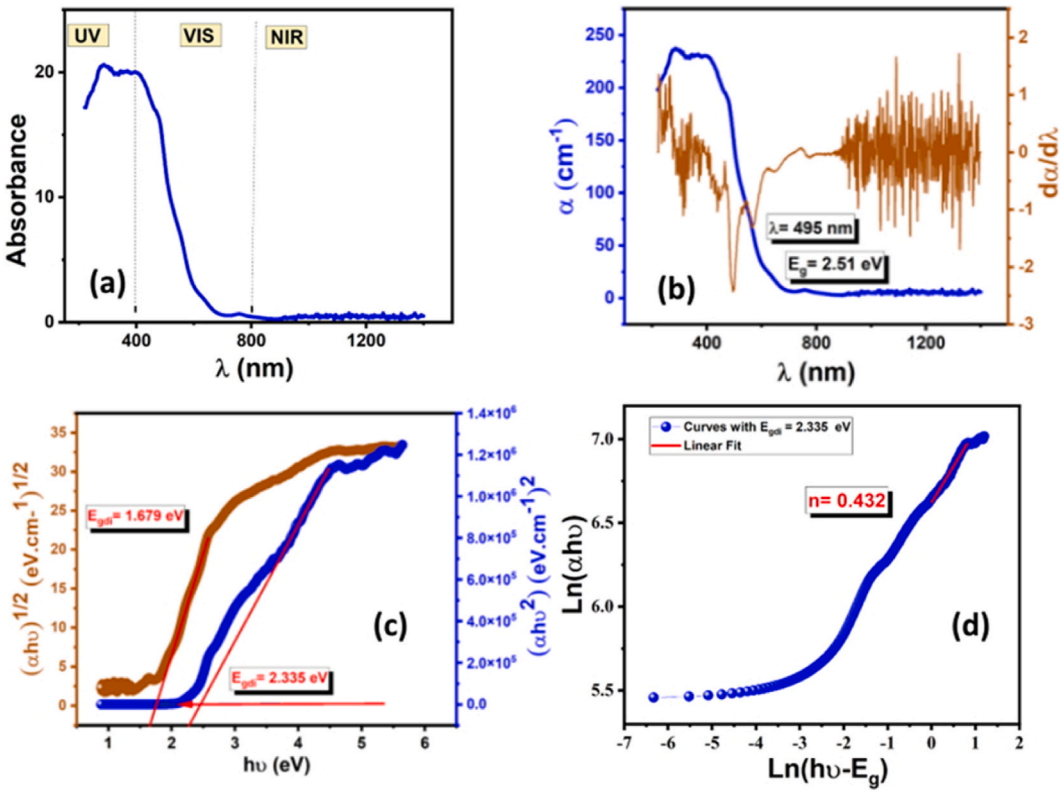

Fig. 8. (a)UV–Vis–NIR spectrum for $Mg_{0.5}Cu_{0.3}Ni_{0.2}Fe_2O_4$ ferrite. **(b)** The curves of α and its derivative (dα/dλ) as a function of the wavelength λ. **(c)** Plots of $(\alpha h\upsilon)^2$ and $(\alpha h\upsilon)^{1/2}$ versus hυ. **(d)** ln(αhν) plots against ln(hν-Eg).

orbitals and the 3d orbitals of the cations (Fe^{3+}, Ni^{2+}, Cu^{2+}), indicating p-d charge transfer and d-d intersite metal-to-metal charge transfer excitations [24]. The substantial absorption in the UV–VIS range makes $Mg_{0.5}Cu_{0.3}Ni_{0.2}Fe_2O_4$ a material with significant potential for photonics and optoelectronics, especially as photovoltaic cells, enabling enhanced light absorption and improved efficiency of energy conversion. Furthermore, its capacity to absorb UV and VIS light makes it a potential photocatalyst, facilitating chemical reactions under light irradiation, which is advantageous for advanced environmental and energy-related applications.

The Beer-Lambert law was employed to determine the optical absorption coefficient, α, from the measured absorbance [24–26].

$$\alpha = \frac{A\ .\ 2.303}{t} \tag{5}$$

A representing the absorbance and *t* the thickness of the sample. The bandgap energy E_g of the compound can be determined by plotting $d\alpha/d\lambda$ as a function of wavelength λ. Fig. 8 (b) displays both the curves for both α and $d\alpha/d\lambda$ in function of wavelength λ. From this plot, the bandgap energy is estimated from the λ value corresponding to the minimum of $d\alpha/d\lambda$. At 495 nm occurs the lowest value, which results in an energy gap (E_g) of approximately 2.51 eV.

To investigate whether the optical transition in our compound is direct or indirect and obtain a more accurate value of E_g, we apply Tauc's law [25]:

$$(\alpha h\nu)^{1/n} = \beta(h\nu - E_g) \tag{6}$$

The incident photon energy is represented by $h\nu$, while β is a parameter reflecting the disorder's degree in the compound. E_g, optical band gap, is determined based on the exponent *n*, which provides information on optical transition nature: $n = 0.5$ *related* to a direct allowed transition, whereas $n = 2$ indicates an indirect allowed transition. In a direct allowed transition, electrons can move directly from the valence to the conduction band bypassing intermediate energy levels.

Fig. 8c presents the plots of $(\alpha h\nu)^{1/2}$ and $(\alpha h\nu)^2$ in function of $h\nu$. Trough extrapolation of the linear region of each curve to the energy axis, the optical band gap was determined using two different approaches: a direct band gap (E_{gd}) and an indirect band gap (E_{gi}). The calculated values are $E_{gd} = 2.335$ eV and $E_{gi} = 1.679$ eV for direct and indirect transitions, respectively.

The value obtained for the direct bandgap is consistent with the value given by the minimum value of the $d\alpha/d\lambda$ curve. It seems then that the optical transition for $Mg_{0.5}Cu_{0.3}Ni_{0.2}Fe_2O_4$ is a direct one.

To check on the type of the optical transition, the Tauc method was applied in its logarithmic form:

$$ln(\alpha h\nu) = nln(\beta) + n\ ln(h\nu - E_g) \tag{7}$$

By using a test band gap energy value of 2.335 eV, Fig. 8d shows the $\ln(\alpha\ h\nu)$ as a function of $\ln(h\nu\text{-}E_g)$. The linear fitting of the curve allowed us to determine the exponent *n*, which was found to be 0.432, i.e., close to 0.5 and supporting that the material exhibits a direct optical transition. This means that electrons can transition directly from the valence to the conduction band without passing through intermediate levels. This property, coupled with its excellent optical absorption and emission features, makes our material a promising candidate in applications such as solar cells, lasers, and optoelectronic devices.

Urbach energy is a characteristic parameter that quantifies the extent of imperfections, impurities, and structural disorder in a material. It originates from localized states within defective regions and manifests as an exponential tail in the absorbance spectrum. By influencing electronic transitions in both the valence and conduction bands, it significantly influences the material's optical properties. The Urbach energy (E_u) of the compound was calculated using the Urbach-Martienssen model [26]:

$$\alpha = \alpha_0 \, exp\left(\frac{h\upsilon - Eg}{E_u}\right) \tag{8}$$

where α_0 is a constant. Taking the logarithms of the above, we get the following relation:

$$\ln(\alpha) = ln(\alpha_0) + \frac{(h\upsilon - E_g)}{E_u} \tag{9}$$

As illustrated in Fig. 9, plotting ln(α) in function of $(h\upsilon$- $Eg)$ allows the E_u as being 0.2386 eV. This outcome reflects a relatively low degree of structural disorder, suggesting a high crystalline quality [27]. This is consistent with the structural analysis reported in Section 3.1.

The Urbach energy (E_u) is associated with the steepness parameter S and may be expressed by the following equation [27,28].

$$E_u = \frac{K_B T}{S} \tag{10}$$

in Eq (10), k_B is the Boltzmann constant, and T denotes the room temperature (approximated as 300 K). Steepness parameter S quantifies absorption edge broadening from electron-phonon or exciton-phonon interactions. The steepness parameter S characterizes how rapidly the absorption coefficient varies with photon energy in the vicinity of the band edge. A high S value signifies a steep absorption edge, while a low S value indicates a more gradual transition. In the case of our sample, the S parameter is 0.11, suggesting a moderate expansion of the absorption edge.

Table 5 clearly shows that our $Mg_{0.5}Cu_{0.3}Ni_{0.2}Fe_2O_4$ sample possesses a distinctive combination of structural and optical properties compared to other ferrite systems. In particular, the synergistic Cu/Ni doping results in a direct bandgap value (2.335 eV) that is intermediate between Cu and Ni-doped ferrites, while maintaining a relatively low Urbach energy, indicating high crystallinity despite the dual doping.

Furthermore, the maximum wavelength of incident radiation, also known as the threshold wavelength (λ_T), is a key criterion for examining the suitability of a material in optoelectronic devices. To estimate λ_T the following expression is used [35]:

$$\left(\frac{A}{\lambda}\right)^2 = C\left(\frac{1}{\lambda}\right) - \left(\frac{1}{\lambda_T}\right) \tag{11}$$

where λ represents the wavelength, C is an empirical constant, and A denotes the absorbance. The inset of Fig. 9 illustrates the plot of $(\alpha/\lambda)^2$ in function of $1/\lambda$. By the tangent drawn at the inflection point of the curve, the value of λ_T was found to be approximately 480 nm. This value indicates that the material begins to absorb significantly in the visible region, making it potentially useful for optoelectronic applications such as detection or light energy conversion.

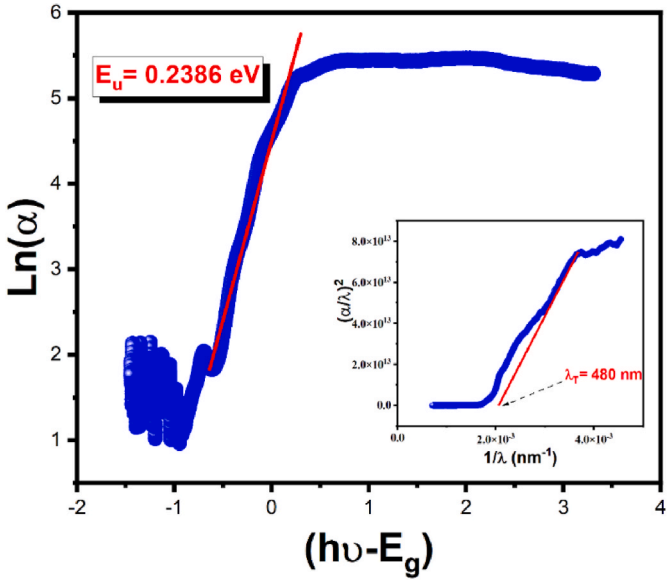

Fig. 9. *Determination of the Urbach energy. The inset show the curve of* $(\alpha/\lambda)^2$ *vs.* $1/\lambda$

The penetration depth (δ) is a crucial parameter to examine a material's capacity to absorb incident radiation. It represents the distance where light intensity drops to 1/e of its surface value [24] and may be estimated as:

$$\delta = \frac{1}{\alpha} \tag{12}$$

The attenuation of radiation within the material can also be evaluated through the optical extinction coefficient k(λ) [24], and is directly correlated to the absorption coefficient α(λ) by the equation:

$$k = \frac{\alpha\lambda}{4\pi} \tag{13}$$

The simultaneous variation of penetration depth and extinction coefficient as a function of wavelength provides valuable insights into light absorption and energy dissipation mechanisms within the material. These parameters are influenced by factors such as thickness, surface roughness, and intrinsic optical properties.

Fig. 10 illustrates the variation of these optical parameters with photon energy, revealing distinct behaviors. Clearly, the penetration depth gradually increases with increasing photon energy, ranging from approximately 0.0042 cm^{-1} to 0.0051 cm^{-1}. This trend indicates a decrease in light absorption at higher energies, reflecting an increase in the material's transparency. Meanwhile, the extinction coefficient shows a significant decrease with increasing photon energy, reaching very low values on the order of 6×10^{-4}, which suggests minimal attenuation of the incident radiation. This optical behavior highlights the low absorption and scattering losses in the high-energy region, confirming the transparent nature of the studied material. These characteristics are particularly advantageous for optoelectronic and photodetection applications, where efficient light management is essential.

Fig. 11 illustrates the evolution of optical conductivity $\sigma_{op}(\lambda)$ for the spinel ferrite $Mg_{0.5}Cu_{0.3}Ni_{0.2}Fe_2O_4$, which is described by the following equation:

$$\sigma_{op} = \frac{\alpha(\lambda)n(\lambda)c}{4\pi k(\lambda)} \tag{14}$$

where n, α, c and k represent the refractive index, absorption coefficient, speed of light, and extinction coefficient, respectively. The results indicate that σ_{op} is higher at low wavelengths and gradually decreases as λ increases. This behavior implies a strong photo-induced response of the material, attributed to the enhanced absorption of high-energy photons, which facilitates electron excitation.

Furthermore, dielectric permittivity is a key element that describes the interaction of the material with an electric or an electromagnetic field. It may be determined using the values of n and k according to the following equation:

$$\varepsilon(\lambda) = [n(\lambda) - ik(\lambda)]^2 = \varepsilon_1(\lambda) - i\varepsilon_2(\lambda) \tag{15}$$

Thus, the real and imaginary parts of dielectric permittivity are expressed as:

$$\varepsilon_1(\lambda) = n^2(\lambda) - k^2(\lambda)$$

$$\varepsilon_2(\lambda) = 2n(\lambda)k(\lambda)$$

Analyzing the curves, it is observed that the dielectric constants increase with wavelength. Additionally, as a result of the small extinction coefficient $k(\lambda)$ values, the variation of $\varepsilon_1(\lambda)$ closely follows that of $n(\lambda)$, while $\varepsilon_2(\lambda)$ exhibits a slight increase with λ.

Table 5
Comparison of structural and optical parameters of $Mg_{0.5}Cu_{0.3}Ni_{0.2}Fe_2O_4$ with similar ferrite systems.

Material	Synthesis method	Grain size (nm)	Lattice parameter (Å)	Direct bandgap (eV)	Urbach energy (eV)	Ref.
$Mg_{0.5}Cu_{0.3}Ni_{0.2}Fe_2O_4$	Sol-gel auto-combustion	1100	8.375	2.335	0.2386	This work
$MgFe_2O_4$	Sol-gel	45	8.383	2.18	0.285	[28]
$Mg_{0.8}Cu_{0.2}Fe_2O_4$	Co-precipitation	38	8.369	2.25	0.267	[29]
$Mg_{0.7}Ni_{0.3}Fe_2O_4$	Hydrothermal	52	8.371	2.21	0.291	[30]
$Mg_{0.6}Cu_{0.2}Ni_{0.2}Fe_2O_4$	Sol-gel	47	8.368	2.28	0.273	[31]
$Mg_{0.5}Zn_{0.5}Fe_2O_4$	Solid state	850	8.397	1.98	0.312	[32]
$CuFe_2O_4$	Sol-gel	32	8.361	2.42	0.198	[33]
$NiFe_2O_4$	Sol-gel	28	8.339	2.51	0.187	[34]

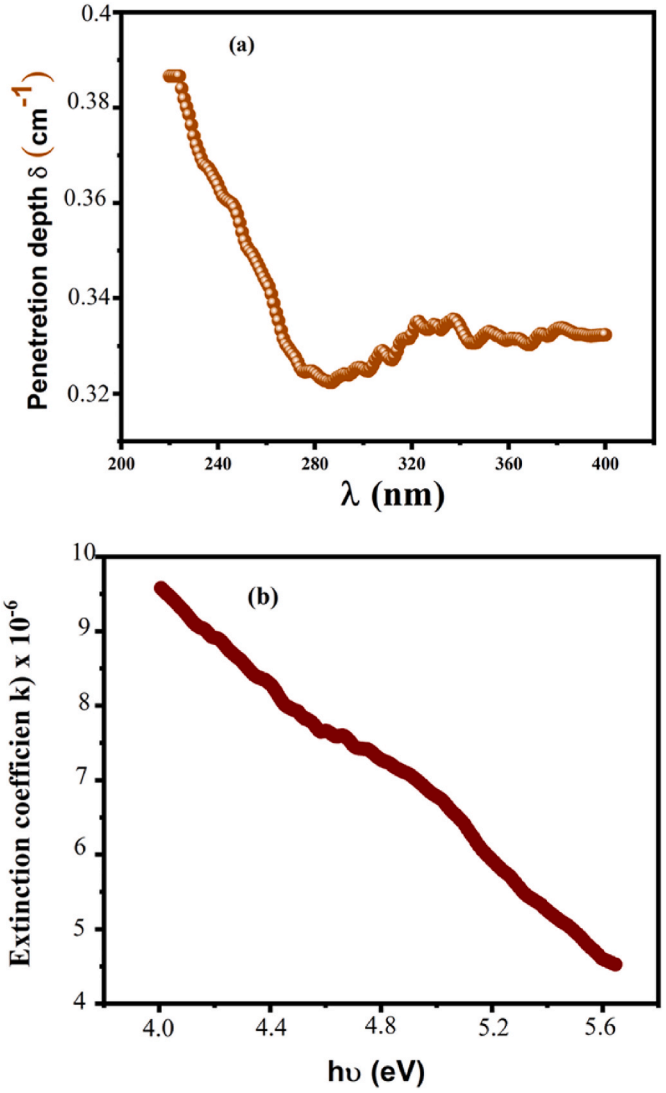

Fig. 10. (a) Penetration depth (δ) versus λ and (b) extinction coefficient (k) versus hν for $Mg_{0.5}Cu_{0.3}Ni_{0.2}Fe_2O_4$.

Finally, the optical loss factor which reflects energy dissipation within the material, is determined using the following equation:

$$\tan(\delta) = \frac{\epsilon_2(\lambda)}{\epsilon_1(\lambda)} \tag{16}$$

Its evolution as a function of λ shows a progressive increase, indicating enhanced optical energy dissipation within the material.

The photoluminescence (PL) of the $Mg_{0.5}Cu_{0.3}Ni_{0.2}Fe_2O_4$ compound was investigated under 300 nm excitation to examine the radiative electronic transitions present in the material. As illustrated in Fig. 12, the resulting PL spectrum displays a wide emission range from 330 to 550 nm, with a maximum intensity around 340 nm. This emission is typical of nanostructured spinel ferrites, where transition metal cations (Fe^{3+}, Cu^{2+}, Ni^{2+}) are distributed between tetrahedral and octahedral sites. This cation distribution promotes the production of structural defects such as oxygen vacancies or crystal field distortions, which are responsible for creating intermediate energy levels facilitating radiative recombination. The strong intensity observed inthe ultraviolet region is consistent with the estimated low results for the direct optical band gap ($E_g \approx 2.335$ eV) and Urbach energy ($E_u \approx 0.2386$ eV), indicating a disordered yet optically active crystalline structure. The relatively large crystallite size (~1.1 μm) contributes to reduced grain boundary scattering, which enhances light absorption across the UV–Vis spectrum. The specific cation arrangement also affects the band structure, as the presence of multiple transition metal ions creates intermediate energy levels within the bandgap. This explains the direct bandgap value of 2.335 eV and the strong UV–Vis absorption observed. The low Urbach energy (0.2386 eV) further confirms that despite the dual doping, the material maintains high crystallinity with minimal structural disorder, which is essential for efficient optoelectronic performance. These results confirm the material's ability to absorb light energy effectively and emit a strong luminescent response, reinforcing its potential for applications in optical sensors, photocatalysis, and optoelectronic devices.

3.4. Electrical conductivity studies

Analyzing how electrical conductivity varies with frequency and temperature is an effective approach to understanding the conduction mechanism, specifically the hopping dynamics of ions. In our case, electrical conductivity is largely attributed to the coexistence of iron in two distinct valence states [36].

The electrical conductivity of $Mg_{0.5}Cu_{0.3}Ni_{0.2}Fe_2O_4$ ferrite was investigated across a frequency range of 100 Hz to 1 MHz and within a temperature range of 250 K–350 K, as shown in Fig. 13a. The observed trends show a stable and consistent electrical response. At low frequency, the conductivity reaches plateau, which represents the contribution of charge carriers mainly controlled by grain boundaries. At higher frequencies, conductivity increases, reflecting the contribution of AC conductivity, which is associated to localized charge hopping under an applied electric field.

The Maxwell–Wagner and Koop models are well adapted to this behavior [37], which describe ferrites as comprising conductive grains isolated by resistive grain boundaries. The region of low frequency is dominated by the grain boundary response, whereas at high frequencies, the grains primarily contribute to conduction.A suitable description of the conductivity's frequency-dependent behavior is provided by Jonscher's universal power law [38]:

$$\sigma(w) = \frac{\sigma_s}{1+\tau^2 w^2} + \frac{\sigma_\infty \tau^2 w^2}{1+\tau^2 w^2} + Aw^s \tag{17}$$

Here, $\sigma_s = \sigma_{dc}$ and $\sigma_\infty = \sigma_{ac}$ represent the conductivities at low frequency (L_f) and high frequency (H_f), respectively. **τ**, **s**, and **A** correspond to the characteristic relaxation time, the power-law exponent, and a

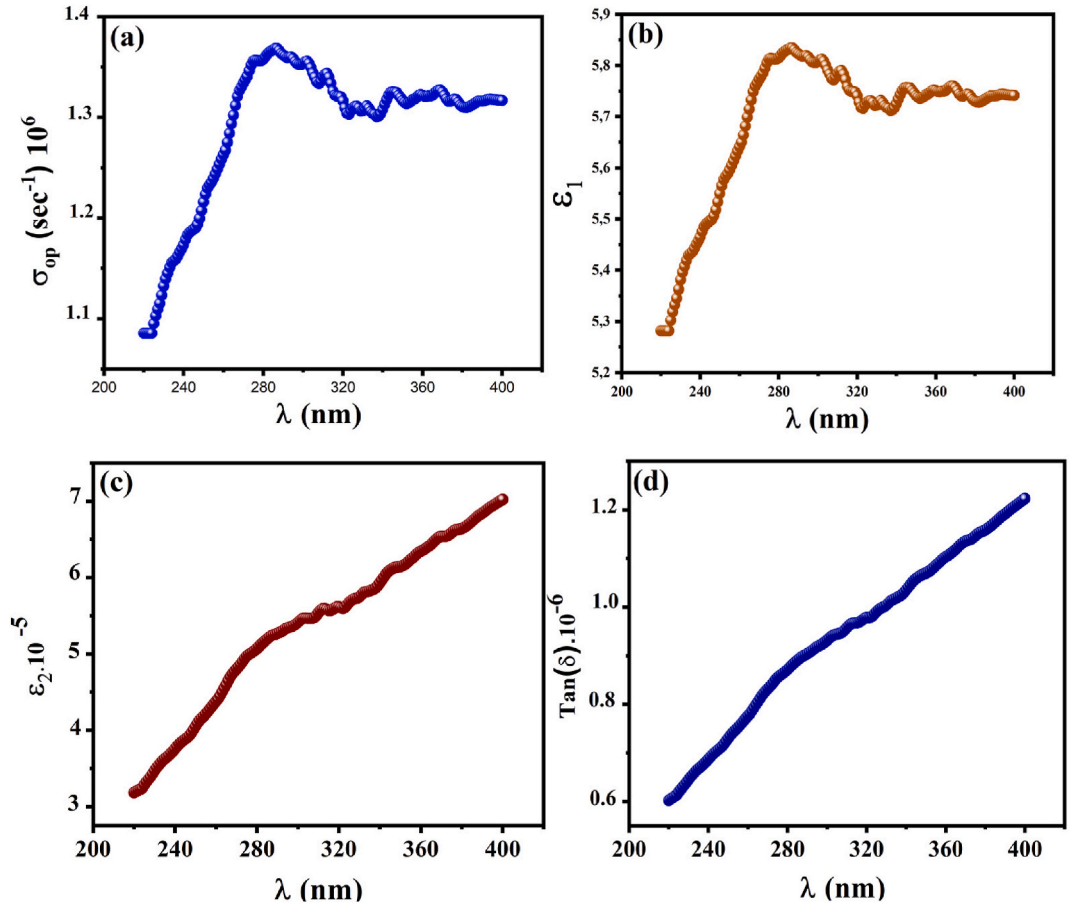

Fig. 11. **(a)** Optical conductivity (σop) versus λ for $Mg_{0.5}Cu_{0.3}Ni_{0.2}Fe_2O_4$ ferrite. **(b)** Real part of dielectric permittivity $\varepsilon 1(\lambda)$. **(c)** Imaginary part of the dielectric permittivity $\varepsilon 2(\lambda)$. **(d)** Variation of the optical loss factor tan(δ) with λ.

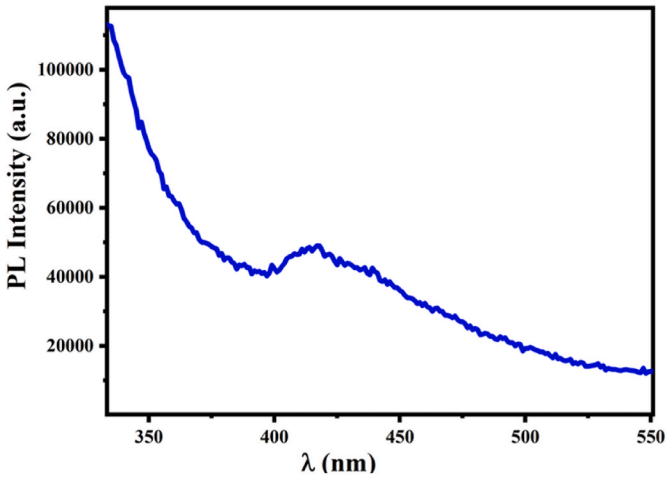

Fig. 12. Wavelength-dependent photoluminescence (PL) spectrum of $Mg_{0.5}Cu_{0.3}Ni_{0.2}Fe_2O_4$ recorded at room temperature.

term that exhibits minimal dependence on temperature, respectively.

The inset in Fig. 13a shows the increase in DC electrical conductivity (σ_{dc}) when temperature increases, which corresponds to a decrease in DC resistivity $\rho_{dc} = \frac{1}{\sigma_{dc}}$. This behavior confirms the semiconducting nature of the compound. The rise in conductivity as temperature increases is attributed to the enhanced mobility of charge carriers, as they gain more thermal energy and overcome potential barriers more easily. Additionally, the synthesized sample exhibits at room temperature a relatively high electrical resistivity, making it a promising candidate for microwave device applications where minimal eddy current losses are desirable [39].

The analysis of the variation of the exponent s(T) with temperature, as shown in Fig. 13b, provides deeper insight into the dominant conduction mechanism in $Mg_{0.5}Cu_{0.3}Ni_{0.2}Fe_2O_4$ [40–42]. The observed decrease in *s* with rising temperature implies that the conduction process is governed by the Correlated Barrier Hopping (CBH) model [43]. This behavior suggests that charge carriers move via hopping between localized states, with thermal energy helping to reduce the potential barriers between these states, thereby facilitating charge transport.

The variation of $\log(\sigma_{dc} \times T)$ is function of $1000/T$ is shown in Fig. 13c according to the following equation:

$$\sigma_{dc} = \frac{\sigma_0}{T} exp\left(-\frac{E_a}{K_B T}\right) \quad (18)$$

The activation energy of the $Mg_{0.5}Cu_{0.3}Ni_{0.2}Fe_2O_4$ compound, determined from DC conductivity measurements, is 0.34 eV, further confirms that the conduction follows a thermally activated mechanism, as described by the Arrhenius law. This activation energy value highlights the influence of the constituent ions within the crystal lattice on charge carrier mobility, which significantly contributes to the electrical properties of the material.

Fig. 14 depicts the AC conductivity as a function of the inverse of the temperature for different applied frequencies. A linear dependence of ln (σ_{ac}*T) on 1000/T is observed, indicating a thermally activated behavior. Each curve exhibits distinct segments corresponding to different temperature ranges, suggesting the presence of various conduction mechanisms. The inset highlights the decrease in activation

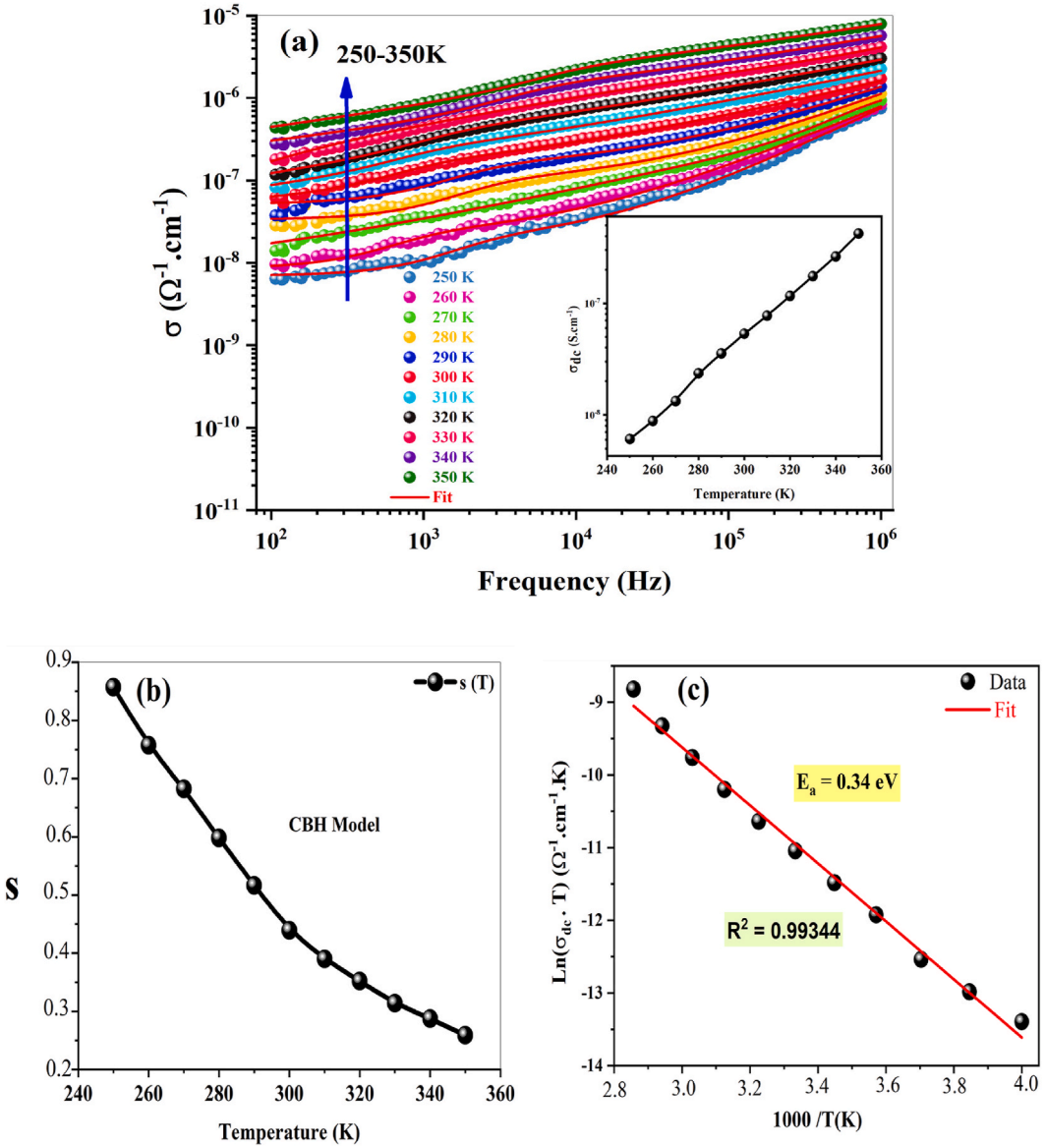

Fig. 13. (a) Frequency variation of conductivity at selected temperatures of $Mg_{0.5}Cu_{0.3}Ni_{0.2}Fe_2O_4$. The inset shows the dc conductivity (σ_{dc}) versus temperature. **(b)** Variation of the exponent S as a function of temperature. **(c)** Variation of Ln (σ_{dc}*T) as a function of 1000/T.

energy (E_a) with increasing applied field frequency. This trend can be explained by an increase in the number of electronic hops between localized states at higher frequencies, promoting a hopping conduction mechanism, which is typical of amorphous or disordered materials.

In summary, the electrical conductivity of $Mg_{0.5}Cu_{0.3}Ni_{0.2}Fe_{2-x}O_4$ ferrites demonstrates a dependence on frequency, temperature, and composition. The results emphasize the suitability of these materials for advanced electronic and microwave applications.

3.5. Dielectric constants

The dielectric properties of this ferrite were evaluated by analyzing the dielectric permittivity (ε' and ε'') and the loss parameter (tan δ) as functions of both frequency and temperature. In general, the variation of the dielectric parameter with frequency results from cumulative contributions, namely electronic, ionic, dipolar, and interfacial polarizations [44].

The dielectric permittivity components, represented by ε' and ε'', are calculated using the expressions:

$$\varepsilon'' = \frac{Z''}{\omega C_0 \left(Z'^2 + Z''^2\right)} \tag{19}$$

$$\varepsilon'' = \frac{Z'}{\omega C_0 \left(Z'^2 + Z''^2\right)} \tag{20}$$

being, $\omega = 2\pi f$ the angular frequency, and C_0 the empty cell capacitance. The real part of permittivity, ε', describes the material's capacity to respond to an electric field without absorbing energy. In contrast, the imaginary part, ε'', indicates the amount of energy the material can absorb from a varying electric field, typically leading to dissipation [45].

Fig. 15(a and b) illustrate the variations of the real part (ε') and the imaginary part (ε'') as functions of angular frequency (between 10 and 10^6 Hz) at different temperatures.

Fig. 15a presents the frequency dependence of the real part of the permittivity he dependence on frequency of the real permittivity part (ε') for the $Mg_{0.5}Cu_{0.3}Ni_{0.2}Fe_2O_4$ sample at various temperatures. The data reveal a pronounced decrease in ε' as the frequency increases, a behavior commonly associated with Maxwell–Wagner interfacial polarization

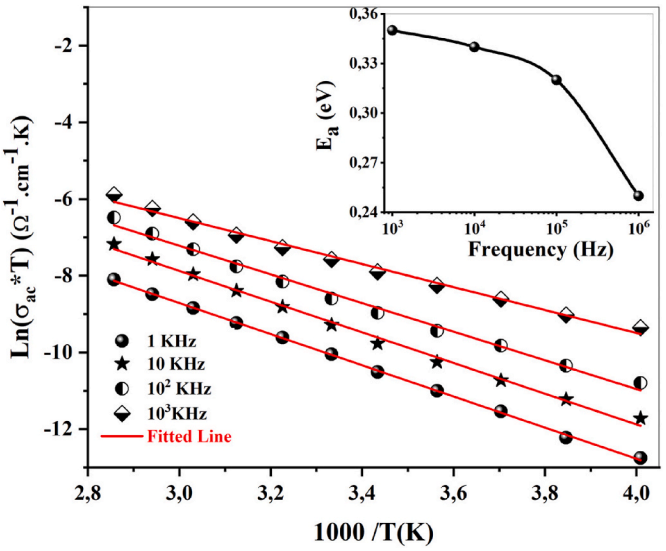

Fig. 14. Ln(σ_{ac}*T) versus 1000/T for the compound $Mg_{0.5}Cu_{0.3}Ni_{0.2}Fe_2O_4$. The inset shows the activation energy (E_a) with increasing applied field frequency.

along with the phenomenological Koop's theory, both of which are typical in ferrite materials. At lower frequencies, ε' shows elevated values due to the contribution of space charge polarization at the grain boundaries, where charge carriers can accumulate and respond to the external electric field. When frequency rises, the capability of these dipoles and charge carriers to follow the rapidly alternating field diminishes, resulting in a sharp decline in ε' and a subsequent stabilization at higher frequencies.

The inset in Fig. 15a further highlights the temperature-dependence of ε', indicating that ε' increases with increasing temperature across the entire frequency range. This enhancement can be attributed to thermally activated charge carriers, which increase the polarization within the material as temperature rises. The observed behavior supports the correlated barrier hopping (CBH) model, as higher temperatures facilitate the movement of charge carriers between localized sites, thereby increasing the dielectric constant.

Overall, the high values of ε' at lower frequencies and elevated temperatures underscore the strong dielectric response and efficient polarization mechanisms in $Mg_{0.5}Cu_{0.3}Ni_{0.2}Fe_2O_4$, making it a promising candidate for applications in energy storage and high-frequency electronic devices, where materials with high permittivity and low dielectric loss are essential. The structural characteristics of $Mg_{0.5}Cu_{0.3}Ni_{0.2}Fe_2O_4$, particularly cation distribution and crystallite size, play a crucial role in determining its functional properties. The confirmed cation distribution $(Fe^{3+})_A[Mg_0^{2+}{}_{.5}Cu_0^{2+}{}_{.3}Ni_0^{2+}{}_{.2}Fe^{3+}]_BO_4^{2-}$ directly influences the material's dielectric behavior. The presence of Cu^{2+} and Ni^{2+} ions predominantly in octahedral sites enhances interfacial polarization due to their different ionic radii (Cu^{2+}: 0.73 Å, Ni^{2+}: 0.69 Å) compared to Mg^{2+} (0.72 Å), creating local lattice distortions that facilitate charge carrier mobility. This explains the observed high dielectric constant ($\varepsilon' > 10^3$) at low frequencies.

Additionally, Fig. 15b illustrates the variation of ε'' with angular frequency (ω) at different temperatures. It is observed that ε'' decreases with increasing frequency until it stabilizes at high frequencies (above 10^3 Hz). This trend can be explained by electron hopping between Fe^{2+} and Fe^{3+} ions. Moreover, the loss of ionic polarization is apparent, as indicated by the substantially high dielectric loss (ε''), observed at lower frequencies. Beyond 10^4 Hz, only the exchangeable ions can follow the applied electric field frequency, leading to a progressive decrease in ε'' across the studied temperature range.

The energy dissipated in a dielectric material under an alternating electric field, is quantified by the dielectric loss factor, tan(δ). This

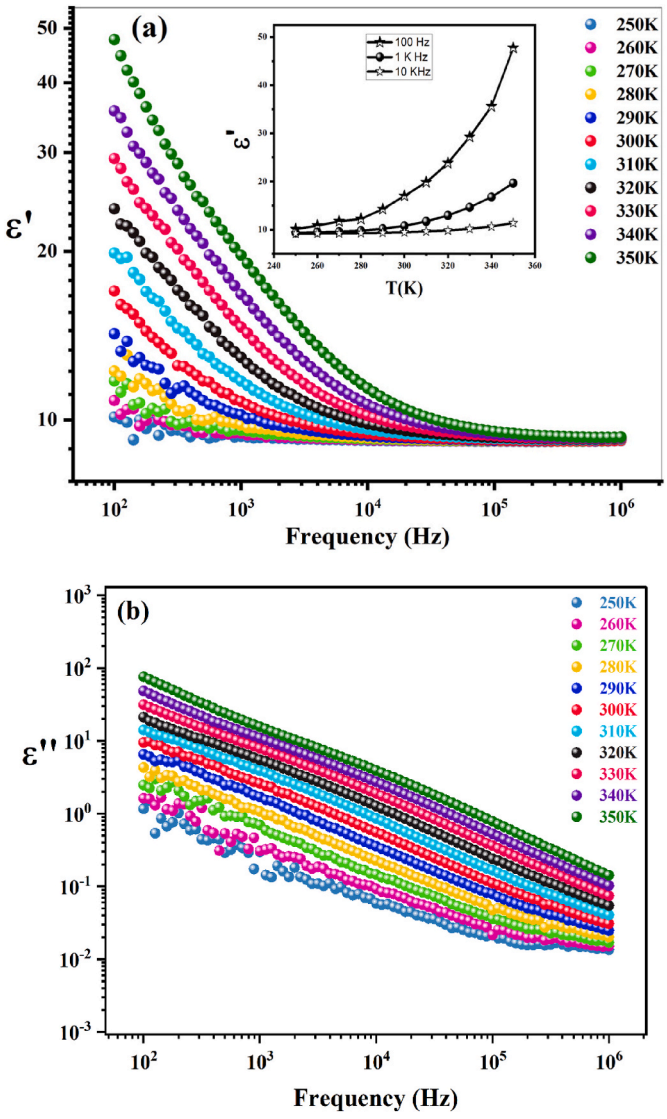

Fig. 15. (a) Variation of the real part, ε', of permittivity with frequency at different temperatures of the $Mg_{0.5}Cu_{0.3}Ni_{0.2}Fe_2O_4$ sample. The inset shows the ε' at different temperatures.**(b)** Variation of the imaginary part, ε'', of permittivity with frequency at different temperatures.

represents the dielectric's ability to dissipate electrical energy as heat. Fig. 16 shows the dielectric loss, calculated by the equation:

$$\tan(\delta) = \frac{\varepsilon''}{\varepsilon'} \tag{21}$$

being ε' and ε'' the real and imaginary components of dielectric constant.

At low frequency, more energy is required to mobilize the charge carriers, leading to an increase in the values of tan(δ). This phenomenon is directly related to the high resistivity of grain boundaries in this frequency range, which limits electrical conduction. In contrast, as the frequency rises, the resistivity of the samples diminishes, facilitating the movement of charge carriers and consequently reducing the dielectric loss factor. Indeed, at low frequencies, the grain boundaries with higher resistivity dominate, leading to enhanced interfacial polarization and a high dielectric constant. As frequency increases, grains control the response, resulting in decreased permittivity and loss. The relaxation time and hopping frequency of charge carriers govern the dielectric relaxation process, with faster hopping occurring at higher temperatures and frequencies. The observed dielectric loss exceeding the dielectric

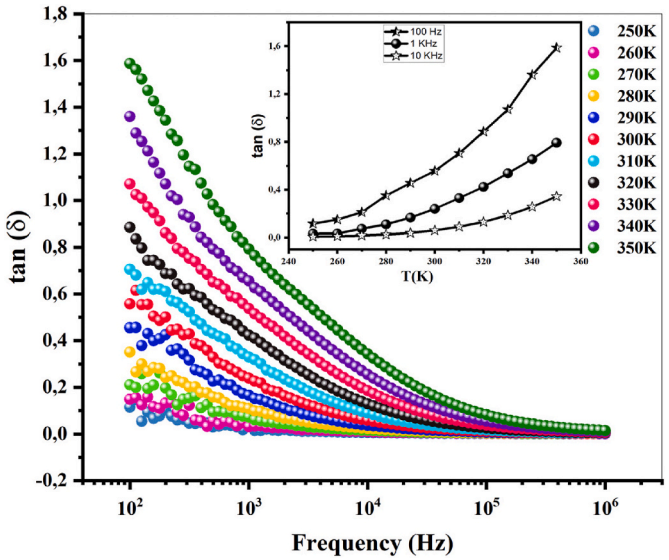

Fig. 16. Variation of the tan(δ) with frequency at different temperatures of the $Mg_{0.5}Cu_{0.3}Ni_{0.2}Fe_2O_4$ sample. The inset shows the dielectric loss tan(δ) at different temperatures.

constant at certain frequencies reflects energy dissipation through charge carrier hopping and conduction mechanisms. This behavior is typical in doped spinel ferrites and aligns well with Maxwell-Wagner interfacial polarization theory. This behavior indicates that the $Mg_{0.5}Cu_{0.3}Ni_{0.2}Fe_2O_4$ ferrite exhibits low dielectric loss at high frequency, making it an attractive candidate for energy transmission and storage uses in these frequency ranges.

The inset of Fig. 16 clearly demonstrates the evolution of dielectric loss, (tan δ) with temperature for the $Mg_{0.5}Cu_{0.3}Ni_{0.2}Fe_2O_4$ sample. As the temperature increases, a noticeable rise in tan δ is observed across the measured frequency range. This trend can be attributed to the enhanced thermal activation of charge carriers, which increases their mobility and facilitates electronic conduction within the spinel lattice. At elevated temperatures, electrons gain sufficient energy to overcome potential barriers, leading to more frequent hopping between localized states, as described by the correlated barrier hopping (CBH) model. Consequently, this increased charge carrier activity results in higher dielectric losses. Similar temperature-dependent behavior of tan δ has been reported in other spinel ferrite systems, further confirming that thermal effects play a crucial role in governing dielectric relaxation and loss mechanisms. The results obtained in this study are consistent with previous reports highlighting the beneficial effect of metal doping on the optical and dielectric properties of ferrites. For instance, the incorporation of Cu^{2+} into the $MgFe_2O_4$ structure has been shown to reduce the optical bandgap due to the formation of localized states between the valence and conduction bands, thereby enhancing visible light absorption [46,47]. Similarly, Mg–Co ferrites co-doped with Cu–Cr exhibit a decrease in E_g correlated with microstructural evolution, along with a significant improvement in dielectric constant and reduced losses at high frequency. These observations confirm that the Cu–Ni co-doping applied in our work follows a similar trend while providing a marked functional gain compared to individually doped systems.

Despite the increase in dielectric loss with temperature, the values remain within an acceptable range at higher frequencies, indicating that the material retains its potential for high-frequency electronic uses where both high permittivity and controlled dielectric losses are essential.

3.6. Complex electrical modulus study

The analysis of the complex electric modulus is really effective for identifying the true origin of ion relaxation behavior. It also has an important role in interpreting the dynamic mechanisms of charge transport in spinel ferrite materials. Additionally, dielectric constants can be utilized to assess the real (M′) and imaginary (M″) parts of the electrical modulus, which are determined using specific mathematical expressions:

$$M' = \frac{\varepsilon'}{(\varepsilon'^2 + \varepsilon''^2)'} \tag{22}$$

$$M'' = \frac{\varepsilon''}{(\varepsilon'^2 + \varepsilon''^2)} \tag{23}$$

These modulus components offer significant understanding of the electrical properties of the sample, including the presence of relaxation processes, and charge carrier dynamics.

Fig. 17(a and b) shows the real (M') and the imaginary (M'') components of the electric complex modulus in function of the frequency at different temperatures.

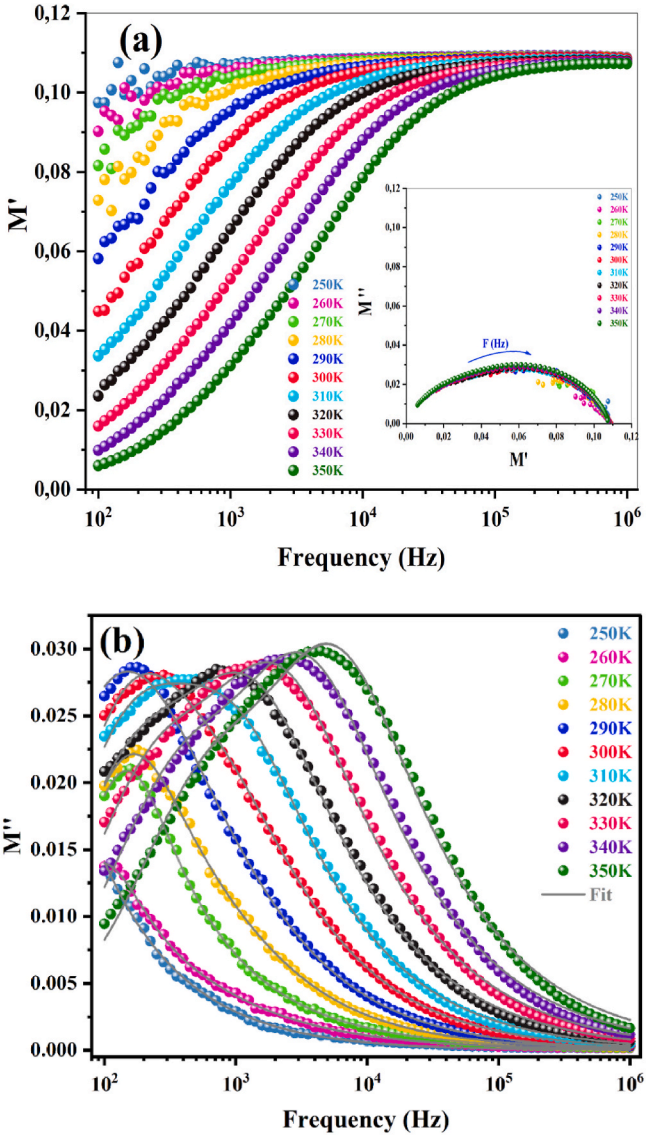

Fig. 17. (a) Frequency dependence at different temperatures of real part (M′) of electrical modulus of the $Mg_{0.5}Cu_{0.3}Ni_{0.2}Fe_2O_4$ sample. The inset shows the complex modulus spectrum of the material at different temperatures. **(b)** Frequency dependence at different temperatures of imaginary part (M″) of electrical modulus.

The spectra exhibit three distinct regions Fig. 17 (a). At low frequencies (LF), the value of M′ is approximately zero, indicating slight contribution from electrode polarization within the material. When frequency increases, M′ rises too, showing the short-range mobility of charge carriers, which serves as the conduction mechanism. Eventually, at high frequencies (HF), M′ stabilizes at a maximum value, suggesting that charge carriers become mobile over longer distances [48]. This trend toward saturation supports the hypothesis that the conduction mechanism is primarily driven by the charge carriers mobility at different frequency ranges.

For a complementary study of the electric modulus, the above mentioned curves, M″(f), were fitted according to the Kohlrausch-Williams-Watts (KWW) equation [49] as shown in the inset of Fig. 16a:

$$M'' = \frac{M''_{max}}{\left[1 - \beta + \left(\frac{\beta}{1+\beta}\right)\left(\beta\left(\frac{f_{max}}{f}\right) + \left(\frac{f}{f_{max}}\right)^{\beta}\right)\right]^{'}} \quad (24)$$

where Mmax′ represents the value of M″ at the highest peak, and β is the stretching factor, which characterizes the type of relaxation in the samples.

The inset of Fig. 17 presents the Cole-Cole plot of the complex modulus, M″ versus M′, for the $Mg_{0.5}Cu_{0.3}Ni_{0.2}Fe_2O_4$ sample at various temperatures. Notably, all the curves corresponding to different temperatures are perfectly superimposed, forming a single, well-defined semicircular arc. This remarkable overlap reflects that the relaxation mechanism governing the dielectric response remains unchanged across the entire temperature range investigated. The presence of a single semicircular arc indicates a narrow distribution of relaxation times and points to a dominant, temperature-independent relaxation process, most likely associated with the intrinsic response of the grains rather than grain boundaries or structural defects. The absence of significant shifts, broadening, or distortion of the arcs with increasing temperature further highlights the homogeneity and stability of the dielectric relaxation dynamics in this material. Such behavior is highly desirable for electronic applications, as it ensures reliable and reproducible dielectric properties under varying thermal conditions, making $Mg_{0.5}Cu_{0.3}Ni_{0.2}Fe_2O_4$ a promising candidate for applications in high-frequency and temperature-stable electronic devices.

The frequency dependence of M″ (Fig. 17b) shows an increase with frequency, except for the peaks observed at high frequencies (HF), which indicates a high-frequency relaxation response in our samples. In the low-frequency (LF) region, below the peak maximum, charge carriers are able to move over long distances. However, on the high-frequency side of the peak, charge carriers are confined locally in their potential wells and can only move over short distances.

The relaxation time, τ, was estimated from the peak maximum, and plotted in accordance to the Arrhenius formula:

$$\tau = \tau_0 \, exp\left(\frac{E_a}{K_B T}\right) \quad (25)$$

Fig. 18 presents a comprehensive investigation of relaxation dynamics in the $Mg_{0.5}Cu_{0.3}Ni_{0.2}Fe_2O_4$ compound, examining the temperature dependence of relaxation time (τ). The observed exponential decrease of τ(T) follows a classical Arrhenius behavior, characteristic of a thermally activated process. Analysis of the temperature dependence through the ln(τ) versus 1000/T plot yields an activation energy E_a = 0.32 ± 0.02 eV. This relatively low value is typical of electron hopping conduction mechanisms between equivalent metal sites in the spinel structure, primarily localized at octahedral positions.

The Arrhenius relation demonstrates exceptional linearity (R^2 = 0.998) across the entire studied temperature range (200–400 K), confirming a single, well-defined relaxation mechanism. This perfect fit to the Arrhenius model indicates the relaxation process is entirely governed by a unique energy barrier of 0.32 eV, characteristic of electron hopping between octahedral sites in the spinel structure. The remarkable stability of this behavior throughout the temperature range highlights the material's homogeneity and the absence of phase transitions or changes in conduction mechanisms within this interval.

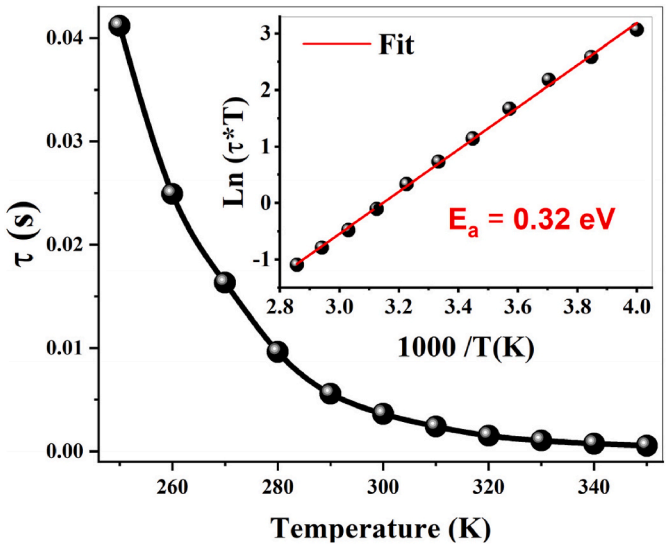

Fig. 18. Variation of log(τ) versus 1000/*T* for the $Mg_{0.5}Cu_{0.3}Ni_{0.2}Fe_2O_4$ sample.

Comparative analysis with similar systems shows the obtained E_a value falls between those reported for $MgFe_2O_4$ (0.38 eV) [50] and $CuFe_2O_4$ (0.29 eV) [51], highlighting the impact of tripartite cation substitution on transport properties. This reduced activation energy, combined with thermal stability up to 450 K, makes this material promising for high-frequency electronic applications where low energy dissipation and controllable relaxation times are crucial. The consistency between different experimental techniques (electric modulus analysis, impedance spectroscopy) reinforces the reliability of these results and opens new perspectives for optimizing these functional materials.

4. Conclusion

In this study, the $Mg_{0.5}Cu_{0.3}Ni_{0.2}Fe_2O_4$ spinel ferrite was successfully synthesized via the sol-gel method, resulting in a single-phase cubic structure with high crystallinity. Structural analyses confirmed the proper cation distribution, which is crucial for ensuring stable physical properties. Optical investigations revealed a direct band gap (Eg ≈ 2.335 eV), low Urbach energy (Eu ≈ 0.2386 eV), and strong UV–Vis absorption, highlighting the material's potential for optoelectronic and light energy conversion applications.

Electrical and dielectric measurements showed semiconducting behavior governed by the Correlated Barrier Hopping (CBH) model, a low activation energy (Ea = 0.34 eV), high permittivity, and low dielectric losses at high frequencies. These characteristics make the material highly suitable for energy storage, high-frequency transmission, and microelectronic device applications.

The combined Cu/Ni doping plays a critical role in tailoring the properties of $MgFe_2O_4$ ferrites. Cu^{2+} ions, due to their larger ionic radius and Jahn–Teller activity, introduce local lattice distortions that enhance optical absorption and carrier mobility. Meanwhile, Ni^{2+} ions contribute to improved structural stability and dielectric behavior. This synergistic effect enables precise control over structural, optical, and electrical properties. Overall, the results demonstrate that Cu and Ni co-doping is an effective strategy for engineering multifunctional spinel ferrites aimed at advanced electronic, optoelectronic, and energy-related technologies.

CRediT authorship contribution statement

Siwar Dhahri: Writing – review & editing, Writing – original draft, Formal analysis, Data curation. **Aref Omri:** Writing – review & editing, Validation, Supervision, Methodology, Formal analysis, Data curation, Conceptualization. **Mohamed Houcine Dhaou:** Formal analysis. **Essebti Dhahri:** Writing – review & editing, Validation. **Manuel P.F. Graça:** Writing – review & editing, Validation, Investigation. **Anna B. Brito:** Investigation. **Rui Fausto:** Writing – review & editing, Validation. **João Pina:** Writing – review & editing, Validation, Investigation, Formal analysis. **Benilde F.O. Costa:** Writing – review & editing, Validation, Supervision, Methodology, Investigation, Funding acquisition, Formal analysis, Data curation, Conceptualization.

Data availability statement

The data that support the findings of this study are available from the corresponding author upon reasonable request.

Declaration of competing interest

The authors declare no conflicts of interest.

Acknowledgements

This work was supported by FCT - Fundação para a Ciência e Tecnologia, I.P. through the projects UIDB/04564/2020 and UIDP/04564/2020, with DOI identifiers 10.54499/UIDB/04564/2020 and 10.54499/UIDP/04564/2020, respectively. Access to TAIL-UC facility funded under QREN-Mais Centro Project No. ICT_2009_02_012_1890 is gratefully acknowledged. R.F. thanks the funding provided by the European Research Agency (European Union) through the Horizon-Widera-2023-Talents-01 ERA-Chair 1011848998: Spectroscopy@IKU "*Manipulating and Characterizing Molecular Architectures: From Isolated Molecules to Molecular Crystals*". The CQC-IMS is supported by FCT through projects UI0313B/QUI/2025, UI0313P/QUI/2025 and LA/P/0056/2020.

References

[1] A. Omri, E. Dhahri, B.F.O. Costa, M.A. Valente, Structural, electric and dielectric properties of Ni0. 5Zn0. 5FeCoO4 ferrite prepared by sol-gel, J. Magn. Magn Mater. 499 (2020) 166243.
[2] M. Horchani, A. Omri, A. Benali, M.S. Eddine, A. Tozri, E. Dhahri, M.F.P. Graca, M. A. Valente, S.K. Jakka, B.F.O. Costa, Synthesis and investigation on the microstructural and electrical proprieties of Ni0.1Co0.5Cu0.4Fe2O4 ferrite prepared using sol-gel route, J. Solid State Chem. 308 (2022) 122898.
[3] S.P. Dalawai, S. Kumar, M.A.S. Aly, M.Z.H. Khan, R. Xing, P.N. Vasambekar, S. Liu, A review of spinel-type of ferrite thick film technology: fabrication and application, J. Mater. Sci. Mater. Electron. 30 (2019) 7752–7779.
[4] A. Selmi, S. Hcini, H. Rahmouni, A. Omri, M.L. Bouazizi, A. Dhahri, Synthesis, structural and complex impedance spectroscopy studies of Ni0. 4Co0. 4Mg0. 2Fe2O4 spinel ferrite, Phase Transitions 90 (10) (2017) 942–954.
[5] M. Kurian, S. Thankachan, Structural diversity and applications of spinel ferrite core-Shell nanostructures-A review, Open Ceramics 8 (2021) 100179.
[6] M. Bourouina, A. Krichene, N. Chniba Boudjada, M. Khitouni, W. Boujelben, Structural, magnetic and magnetocaloric properties of nanostructured $Pr_{0.5}Sr_{0.5}MnO_3$ manganite synthesized by mechanical alloying, Ceram. Int. 43 (2017) 8139–8145.
[7] A. Messaoudi, A. Omri, N. Hamdaoui, A. Benali, R. Ajjel, M.F.P. Graca, B.F. O. Costa, K. Khirouni, Advanced spinel ferrite Co0. 6Zn0. 3Ca0. 1Fe2O4 nanoparticles: structural, optical, and electrical insights for functional applications, Journal of the Australian Ceramic Society (2025) 1–20.
[8] P. Jadoun, J. Sharma, S. Kumar, S.N. Dolia, D. Bhatnagar, V.K. Saxena, Structural and magnetic behavior of nanocrystalline Cr doped Co-Mg ferrite, Ceram. Int. 44 (6) (2018) 6747–6753.
[9] G. Mustafa, M.U. Islam, W. Zhang, Y. Jamil, A.W. Anwar, M. Hussain, M. Ahmad, Investigation of structural and magnetic properties of Ce3+-substituted nanosized Co–Cr ferrites for a variety of applications, J. Alloys Compd. 618 (2015) 428–436.
[10] J. Pei, Z. Wang, Y. Gao, H. Zhang, Structure and magnetic properties of Ni0. 5Zn0. 5Mn0. 5-xMoxFe1. 5O4 ferrites prepared by sol-gel auto-combustion method, Curr. Appl. Phys. 19 (4) (2019) 440–446.
[11] P.P. Hankare, S.D. Jadhav, U.B. Sankpal, S.S. Chavan, K.J. Waghmare, B. K. Chougule, Synthesis, characterization and effect of sintering temperature on magnetic properties of MgNi ferrite prepared by co-precipitation method, J. Alloys Compd. 475 (1–2) (2009) 926–929.
[12] F. Sun, L. Huang, R. Zhang, S. Wang, S. Jiang, Y. Sun, L. Geng, In-situ synthesis and superhigh modulus of network structured TiC/Ti composites based on diamond-Ti system, J. Alloys Compd. 834 (2020) 155248.
[13] T. Bachaga, Mohamed Khitouni Zhang, NiMn-based Heusler magnetic shape memory alloys: a review, Int. J. Adv. Des. Manuf. Technol. 103 (2019) 2761–2772.
[14] X. Zhou, C. Zhang, M. Zhang, A. Feng, S. Qu, Y. Zhang, G. Wu, Synthesis of Fe3O4/carbon foams composites with broadened bandwidth and excellent electromagnetic wave absorption performance, Compos. Appl. Sci. Manuf. 127 (2019) 105627.
[15] D.T. Wiles, R.A. Young, A new computer program for Rietveld analysis of X-ray powder diffraction patterns, Applied Crystallography 14 (2) (1981) 149–151.
[16] D.P. Law, A.B. Blakeney, R. Tkachuk, The Kubelka–Munk equation: some practical considerations, J. Near Infrared Spectrosc. 4 (1) (1996) 189–193.
[17] R.A. Young, D.B. Wiles, Profile shape functions in Rietveld refinements, Applied Crystallography 15 (4) (1982) 430–438.
[18] K. Momma, F. Izumi, VESTA 3 for three-dimensional visualization of crystal, volumetric and morphology data, Applied Crystallography 44 (6) (2011) 1272–1276.
[19] M. Chemingui, R. Ameur, V. Optasanu, M. Khitouni, SC analysis of phase transformations during precipitation hardening in Al–Zn–Mg alloy, J. Therm. Anal. Calorim. 136 (2020) 1887–1894.
[20] A.M. Mansour, M. Morsy, A.M. El Nahrawy, A.B. Abou Hammad, Humidity sensing using Zn (1.6−x) Na0.4CuxTiO4 spinel nanostructures, Sci. Rep. 14 (1) (2024) 562.
[21] K. Sabri, A. Rais, K. Taibi, M. Moreau, B. Ouddane, A. Addou, Structural Rietveld refinement and vibrational study of MgCrxFe2− xO4 spinel ferrites, Phys. B Condens. Matter 501 (2016) 38–44.
[22] A. Turkin, V. Drebushchak, Y. Kovalevskaya, I. Paukov, Low-temperature heat capacity of magnesioferrite, MgFe 2 O 4, J. Therm. Anal. Calorim. 92 (3) (2008) 717–721.
[23] O.N. Kondrat'eva, A.V. Khoroshilov, V.A. Ketsko, K.S. Gavrichev, Heat capacity and thermodynamic functions of Mg (Fe 0.8 Ga 0.2) 2 O 4 at high temperatures, Russ. J. Inorg. Chem. 60 (2015) 1544–1547.
[24] N. Missaoui, F. Hcini, O. Amorri, S. Hcini, I. Ghiloufi, J. Dhahri, H. Alsalmah, A. Mimouni, M. Hjiri, K. Khirouni, The influence of calcination temperature on structural, optical, and impedance spectroscopy properties of mixed Ni0. 4Cd0. 3Co0. 3Fe2O4 spinel ferrites synthesized using the sol–gel method, J. Inorg. Organomet. Polym. Mater. 34 (2) (2024) 622–639.
[25] B.F. Costa, A. Benali, B.J. Vieira, J.C. Waerenborgh, J. Pina, Y. Marouani, E. Dhahri, Mössbauer and optical investigations on Sr doped M-type BaFe12O19 Hexaferrites produced via Autocombustion, Crystals 15 (4) (2025) 291.
[26] A. Messaoudi, A. Omri, A. Benali, M.A. Ghebouli, A. Djemli, M. Fatmi, A. Habila, A. A. Alothman, N. Hamdaoui, R. Ajjel, B.F.O. Costa, M.F.P. Graca, K. Khirouni, Prediction study of structural, thermal, and optical characterization of Co0. 6Zn0. 4Fe2O4 cubic spinel synthesized via sol–gel method for energy storage, J. Kor. Phys. Soc. 84 (12) (2024) 958–968.
[27] S. Husain, A.O. Keelani, W. Khan, Influence of Mn substitution on morphological, thermal and optical properties of nanocrystalline GdFeO3 orthoferrite, Nano-Struct. Nano-Objects 15 (2018) 17–27.
[28] R. Srimathi, N.S. Rao, A. Merlin, R. Kiruthika, A. Selvaraj, O.H. Abdelkader, S. Revathi Chandra Sekhar Dash, Anis Ahamed, Ramalingam Rajabathar Jothi, M. Sundararajan, S. Yuvaraj, L. Rajadurai, Investigation of structural, magnetic, optical and dielectric characteristics of Al-doped $MgFe_2O_4$ nanoparticles, Solid State Sci. 159 (2025) 107761.
[29] P. Roy, S.M. Hoque, S. Akter, S.I. Liba, S. Choudhury, Study on the chemical co-precipitation synthesized $CoFe_2O_4$ nanoparticle for magnetocaloric performance in the vicinity of superparamagnetic blocking temperature, Heliyon 10 (14) (2024).
[30] A. Manohar, T. Suvarna, S.P. Vattikuti, A.A. Almunyif, S. Sangaraju, K.H. Kim, Characterization of a synthesized $Mg_{0.7}Ni_{0.3}Fe_2O_4/CeO_2/MgFe_2O_4$ nanocomposite for magnetic and electrochemical applications, Colloids Surf. A Physicochem. Eng. Asp. (2025) 137269.
[31] J. Geng, J. Ma, S. Ma, F. Li, L. Zhang, X. Ning, G.M. Lohar, Energy band investigation and role of Fe content in $Zn_{1-x}Fe_xSe$ based nanomaterials for photoelectrochemical cell application, Ceram. Int. 45 (11) (2019) 14457–14463.
[32] A. Tariq, K. Mehmood, S. Akbar, H.A. Bhatti, M.D. Khan, S. Rashid, Q.U.A. Asif, Optimizing optical, dielectric, structural, and electrical properties in Cu-substituted Mg-Zn ferrite nanoparticles: insights for sustainable energy and environmental solutions, J. Alloys Compd. (2025) 182252.
[33] R. Peymanfar, F. Azadi, Y. Yassi, Preparation and characterization of $CuFe_2O_4$ nanoparticles by the sol-gel method and investigation of its microwave absorption properties at Ku-band frequency using silicone rubber, Proceedings 2 (17) (2018, May) 1155.
[34] A. Abu El-Fadl, A.M. Hassan, M.A. Kassem, Structural and spectroscopic studies of nanocrystalline $Ni_{1-x}Mg_xFe_2O_4$ ferrites synthesized by a microwave-assisted combustion route, Phys. Scr. 95 (2020) 055813.
[35] O. Rejaiba, K. Khirouni, M.H. Dhaou, B. Alzahrani, M.L. Bouazizi, J. Khelifi, Investigation study of optical and dielectric parameters using absorption and diffuse reflectance spectroscopy method on $La_{0.57}Nd_{0.1}Sr_{0.13}Ag_{0.2}$ MnO_3 perovskite for optoelectronic application, Opt. Quant. Electron. 54 (5) (2022) 315.
[36] A. Tozri, E. Dhahri, High-temperature dielectric behavior of hexagonal HoMnO3, J. Phys. Chem. Solid. 152 (2021) 109960.
[37] C.G. Koops, On the dispersion of resistivity and dielectric constant of some semiconductors at audiofrequencies, Physical review 83 (1) (1951) 121.

[38] A. Chouket, O. Bidault, V. Optasanu, A. Cheikhrouhou, M. Khitouni, Enhancement of the dielectric response through Al-substitution in La1.6Sr0.4NiO4 nickelates, RSC Adv. 6 (2016) 24543–24548.
[39] I. Sadiq, S. Naseem, M.N. Ashiq, M.A. Khan, S. Niaz, M.U. Rana, Structural and dielectric properties of doped ferrite nanomaterials suitable for microwave and biomedical applications, Prog. Nat. Sci. Mater. Int. 25 (5) (2015) 419–424.
[40] A.A. Dakhel, The annealing effect for structural, optical and electrical properties of + dysprosium–manganese oxide films grown on Si substrate, Solid State Electron. 49 (12) (2005) 1996–2001.
[41] D.L. Sekulic, Z.Z. Lazarevic, M.V. Sataric, C.D. Jovalekic, N.Z. Romcevic, Temperature-dependent complex impedance, electrical conductivity and dielectric studies of M Fe 2 O 4 (M= Mn, Ni, Zn) ferrites prepared by sintering of mechanochemical synthesized nanopowders, J. Mater. Sci. Mater. Electron. 26 (2015) 1291–1303.
[42] S.R. Elliott, Ac conduction in amorphous chalcogenide and pnictide semiconductors, Adv. Phys. 36 (2) (1987) 135–217.
[43] R. Megha, S. Kotresh, Y.T. Ravikiran, C.V. Ramana, S.C. Vijaya Kumari, S. Thomas, Study of alternating current conduction mechanism in polypyrrole-magnesium ferrite hybrid nanocomposite through correlated barrier hopping model, Compos. Interfaces 24 (1) (2017) 55–68.
[44] T.W. Dakin, Conduction and polarization mechanisms and trends in dielectric, IEEE Electr. Insul. Mag. 22 (5) (2006) 11–28.
[45] A. Candan, A.K. Kushwaha, A first-principles study of the structural, electronic, optical, and vibrational properties for paramagnetic half-Heusler compound TiIrBi by GGA and GGA+ mBJ functional, Mater. Today Commun. 27 (2021) 102246.
[46] D. Mallesh, Naresh Pallati, Aravind Seem, Synthesis, structural, optical, dielectric and AC conductivity studies of nickel Ni doped magnesium nano ferrites for multiple applications, J. of Next Research 2 (1) (2025) 100079.
[47] S. Chandra Devsharma, Md Lutfor Rahman, Md Jakir Hossain, Bristy Biswas, Md Farid Ahmed, Nahid Sharmin, Elucidation of structural, electromagnetic, and optical properties of Cu–Mg ferrite nanoparticles, Heliyon 10 (13) (2024) e33578.
[48] M. Slimi, M. Azabou, L. Escoda, JJ. Khitouni. M. Suñol, Structural and microstructural properties of nanocrystalline Cu–Fe–Ni powders produced by mechanical alloying, Powder Technol. 266 (2014) 262–267.
[49] M. Horchani, M. Seif Eddine, A. Omri, A. Benali, M. Taoufik, E. Dhahri, M. A. Valente, B.F.O. Costa, R. Ben Younes, Microstructural, Mössbauer, thermal and dielectric studies of ZnFeCoO4 spinel oxide for optoelectronic applications, J. Mater. Sci. Mater. Electron. 34 (2023) 1298.
[50] F. Farshad, O. Hannah, H. Dominic Ryan, G. Khashayar, Electrical Effects of Ionic Deficient Cubic Ferrite Spinels: A Case Study on $MgFe_2O_4$, Advanced Physics Research, 2023 2300057.
[51] K. Rouibah, F.-Z. Akika, C. Rouibah, H.-R. Boudermine, S. Douafer, S. Boukerche, G. Boukerche, M. Benamira, Solar photocatalytic degradation of Methyl green on $CuFe_2O_4$/α-Fe_2O_3 heterojunction, Inorg. Chem. Commun. 148 (2023) 110361.